Rapid Nondestructive Analysis of Threading Dislocations in Wurtzite Materials Using the Scanning Electron Microscope

G. Naresh-Kumar,[1] B. Hourahine,[1] P. R. Edwards,[1] A. P. Day,[2] A. Winkelmann,[3] A. J. Wilkinson,[4] P. J. Parbrook,[5,*] G. England,[6] and C. Trager-Cowan[1,†]

[1]*Department of Physics, SUPA, University of Strathclyde, Glasgow G4 ONG, United Kingdom*
[2]*Aunt Daisy Scientific Ltd, Claremont House, High St, Lydney, Gloucestershire, GL15 5DX, United Kingdom*
[3]*Max-Planck-Institut für Mikrostrukturphysik, Weinberg 2, D-06120 Halle, Germany*
[4]*Department of Materials, University of Oxford, Oxford OX1 3PH, United Kingdom*
[5]*Department of Electronic and Electrical Engineering, University of Sheffield, S1 3JD, United Kingdom*
[6]*K.E. Developments Ltd, Cambridge, CB23 2RL, United Kingdom*

(Received 14 October 2011; published 30 March 2012)

We describe the use of electron channeling contrast imaging in the scanning electron microscope to rapidly and reliably image and identify threading dislocations (TDs) in materials with the wurtzite crystal structure. In electron channeling contrast imaging, vertical TDs are revealed as spots with black-white contrast. We have developed a simple geometric procedure which exploits the differences observed in the direction of this black-white contrast for screw, edge, and mixed dislocations for two electron channeling contrast images acquired from two symmetrically equivalent crystal planes whose $\boldsymbol{g}$ vectors are at 120° to each other. Our approach allows unambiguous identification of all TDs without the need to compare results with dynamical simulations of channeling contrast.

DOI: 10.1103/PhysRevLett.108.135503 PACS numbers: 61.72.Ff, 07.78.+s, 61.72.uj, 68.37.Hk

The reduction of defects such as threading dislocations (TDs) in GaN, ZnO, SiC, and related materials is key to the optimization of new devices. TDs act as scattering centers for light and charge carriers and give rise to nonradiative recombination and to leakage currents, severely limiting device performance [1–3].

At present, transmission electron microscopy (TEM) is the best known technique for characterizing individual dislocations [4–6]. The need for sample preparation and the localized nature of the information acquired from TEM make other microscopic imaging techniques such as atomic force microscopy, and the subject of this Letter, electron channeling contrast imaging (ECCI) coupled with the acquisition of electron channeling patterns (ECPs), attractive complementary techniques to TEM.

Electron channeling contrast images are produced from electrons which channel down, or equivalently are diffracted from the crystal planes of a suitably oriented sample. Changes in crystallographic orientation or changes in lattice constant due to local strain are revealed by changes in contrast in a channeling image constructed by monitoring the intensity of backscattered electrons as an electron beam is scanned over the sample. Extremely small changes in orientation and strain are detectable, revealing, for example, low angle tilt and rotation boundaries and atomic steps and enabling dislocations to be imaged. Vertical TDs appear as spots with black-white (B-W) contrast; this is seen in Fig. 1(a), an electron channeling contrast image acquired from a 1600 nm GaN thin film. All images in this Letter were acquired from this sample, the growth conditions for which are reported elsewhere [7].

The conditions required to resolve individual dislocations in an electron channeling contrast image are quite stringent; a small (nanometers), high brightness (nanoamps or higher), low divergence (a few mrad) electron beam is required [8]. Such conditions are met in a field emission gun scanning electron microscope. Our electron channeling contrast images were acquired with an electron beam spot of ≈ 4 nm, a beam current of ≈ 2.5 nA, and a beam divergence of ≈ 4 m rad using an FEI Sirion field emission gun scanning electron microscope. We use a forescatter geometry where the sample is tilted between 30° and 70° to the impinging electron beam and the backscattered electrons are detected by an electron-sensitive diode placed in front of the sample [8,9]. It is also necessary to use a detection system that allows discrimination between electrons leaving the sample which carry channeling

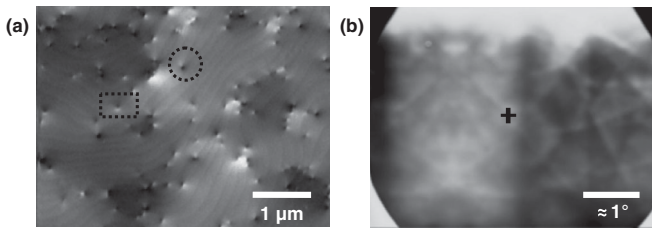

FIG. 1. (a) Multibeam ECC image showing atomic steps and (b) ECP, both acquired at 30 keV. On the ECC image, the dotted circle highlights a dislocation with a screw component and the dotted rectangle highlights an edge dislocation. The cross on the ECP marks the PC.

information and those which have been diffusely scattered by the sample. An amplifier which can offset the diffuse background signal and amplify the channeling signal is required. We use electron-sensitive diodes and a signal amplifier provided by K.E. Developments Ltd.

The acquisition of an electron channeling pattern (ECP) allows the set of planes from which the electrons are diffracted to be selected. This procedure is referred to as selecting $\boldsymbol{g}$. An ECP is obtained when changes in the backscattered electron intensity are recorded as the angle of the incident electron beam is changed relative to the surface of a single crystal area of the sample—this is referred to as *rocking* the beam. When an image is acquired at low magnification, as the beam is scanned over the sample, it changes its angle with respect to the surface of the sample (in our case by around $\pm 2.5°$) allowing an ECP to be obtained. When the beam is rocked over the sample, different planes of the crystal satisfy the Bragg condition, giving rise to the appearance of overlapping bands of bright and dark lines (Kikuchi lines [10]) superimposed on the image of the sample; this is the ECP, as seen in Fig. 1(b). The ECP is a 2D projection of the crystal structure, with the Kikuchi lines corresponding to different planes in the crystal. Comparing the ECP with kinematical electron diffraction [11] simulations allows the pattern to be indexed, that is, the planes in the ECP to be identified. We have also compared our ECPs with dynamical simulations [12] to verify our indexing, as shown in Fig. 2. The point on the ECP around which the electron beam is rocked is referred to as the pattern center (PC) [see Fig. 1(b)]. If a single Kikuchi line intersects the PC, this is the plane which will provide channeling contrast in the electron channeling contrast image. Changing the tilt and/or rotation of the sample allows different $\boldsymbol{g}$ to be selected. If only one Kikuchi line intersects the PC, this is referred to as a two-beam diffraction condition (i.e., only the incident beam and the diffracted beam from one plane determine the contrast in the electron channeling contrast image). If more than one Kikuchi line intersects the PC then we have a multibeam diffraction condition. In general, electron channeling contrast images acquired under multibeam conditions exhibit better signal to noise than those obtained using two-beam conditions. In practice, it is difficult to achieve exact two-beam conditions; however, it is possible to get sufficiently close to allow quantitative analysis of the resultant electron channeling contrast images. Note that the acquisition time required to obtain either an electron channeling contrast image or an ECP is typically less than a minute. Detailed descriptions of ECCI and ECP are given in the references [8,9,12–15].

It is possible to select a diffraction condition (and the position of the forescatter detector) so that atomic steps in the nitride thin films are revealed. The atomic steps are revealed due to lattice distortion at the steps. Similar step contrast is observed in resonance electron microscopy images [16,17]. If a diffraction condition is selected so as to give strong contrast for the atomic steps and for screw, edge, and mixed dislocations (normally a multibeam condition), it is possible to differentiate between dislocations with a screw component (those which terminate a step) and pure edge dislocations (those that do not terminate a step) in a manner analogous to that used to identify dislocations in atomic force microscopy images [18]. This is illustrated in Fig. 1(a). However, this method does not allow discrimination between pure screw and mixed dislocations.

It is possible to identify dislocations in electron channeling contrast images using the invisibility criteria used in TEM [19]. However, for plan-view diffraction images of c-plane-oriented wurtzite materials, it is not possible to satisfy both $\boldsymbol{g} \cdot \boldsymbol{b} = 0$ and $\boldsymbol{g} \cdot \boldsymbol{b} \times \boldsymbol{u} = 0$ (where $\boldsymbol{b}$ is the Burgers vector) for vertical threading edge dislocations ($\boldsymbol{b} = 1/3\langle 11\text{–}20\rangle$); the ideal $\boldsymbol{g}$ to satisfy the invisibility criterion for all edge dislocations is (0002) which is not accessible in the plan-view geometry. For the vertical threading screw dislocations ($\boldsymbol{b} = \langle 0001\rangle$) surface relaxation dominates and again the invisibility criterion cannot be applied. The surface relaxation contrast mechanism was first described by Tunstall *et al* [20], and results from ''a nonuniform twist of the lattice about the screw dislocation, which decreases with increasing distance from the center of the screw''. Where a screw dislocation is revealed by surface relaxation, the B-W contrast direction is perpendicular to $\boldsymbol{g}$.

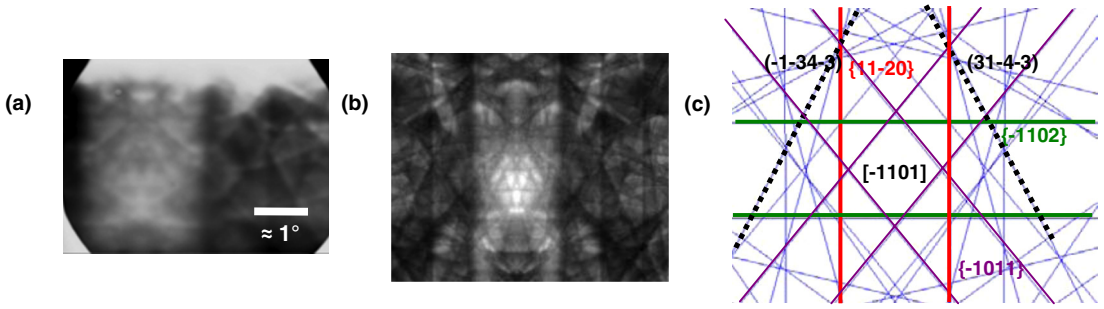

FIG. 2 (color online). (a) Experimental ECP [same as that shown in Fig. 1(b)]. (b) Dynamical simulation of ECP and (c) kinematical simulation of ECP from c-GaN (for an incident electron beam energy of 30 keV).

As it was found not to be possible to identify the dislocations in our GaN thin film by applying the standard TEM invisibility criteria, another approach had to be developed. In this Letter, we describe a procedure which exploits the differences observed in the direction of the B-W contrast for screw, edge, and mixed dislocations on comparing two images acquired via channeling from two symmetrically equivalent crystal planes whose $\boldsymbol{g}$ are at 120° to each other. The diffracting planes were selected to produce similar channeling contrast for the screw, edge, and mixed dislocations. The choice of symmetrically equivalent planes for the acquisition of the two images produces a simple and easily predictable change in the direction of the observed B-W contrast. This procedure allows us to unambiguously identify the individual dislocations. The application of this simple geometric approach does not require the comparison of our experimental images with dynamical simulations of channeling contrast.

To our knowledge, there is no reported work on identifying all the different TD types in wurtzite nitride thin films using ECCI. There have been a number of seminal papers published by Picard *et al* [21,22] in which the authors, following the work of Tunstall *et al* [20], identified dislocations with a screw component as those which exhibited a B-W contrast direction perpendicular to their selected $\boldsymbol{g}$. They selected their $\boldsymbol{g}$ from electron backscatter diffraction patterns. They also identified edge dislocations as those whose B-W contrast was independent of $\boldsymbol{g}$. However, they were not able to differentiate between screw and mixed dislocations, and thus were not able to identify pure screw dislocations which are the most detrimental to the device performance in a wide range of semiconductors [23–26]. The ability to unambiguously differentiate all three types of dislocations places us in an excellent position to understand the role of screw versus mixed versus edge dislocations in the performance of a wide range of devices.

The technique we are using to identify dislocation types in our electron channeling contrast images is simple, but the simplicity of the technique relies on choosing appropriate crystal planes for diffraction. Two symmetrically equivalent crystal planes, (31–4–3) and (–1–34–3), with $\boldsymbol{g}$ at 120° to each are selected (see Fig. 3). Figures 3(a) and 3(b) show the electron channeling contrast images taken from the same part of the sample for the two chosen $\boldsymbol{g}$. To identify the dislocations we monitor the changes in the direction of the B-W contrast that occur when the direction of $\boldsymbol{g}$ is changed. Figures 3(c) and 3(d) show the ECPs which correspond to the electron channeling contrast images of Figs. 3(a) and 3(b), respectively. Note that in each case only a single crystal plane has been chosen for diffraction and hence the intensity and contrast of the observed dislocations are determined by these selected crystal planes; i.e., we are imaging under two-beam diffraction conditions. The circle, rectangle, and the octagon shown in Figs. 3(a) and 3(b) highlight screw, edge, and mixed dislocations, respectively, taken at the two selected $\boldsymbol{g}$. Note that when the diffraction conditions are changed, this also changes contrast in subgrains, i.e., regions bounded by low angle tilt or rotation boundaries. For example, the brighter contrast seen in the top right corner indicated by a black arrow in Fig. 3(a) changes to dark contrast indicated by a white arrow in Fig. 3(b). The dark band which appears across the middle of the image shown in Fig. 3(b) is a ''shadow'' cast by a particle on the surface of the sample. This particle was used to help locate the same part of the sample when the diffraction conditions were changed.

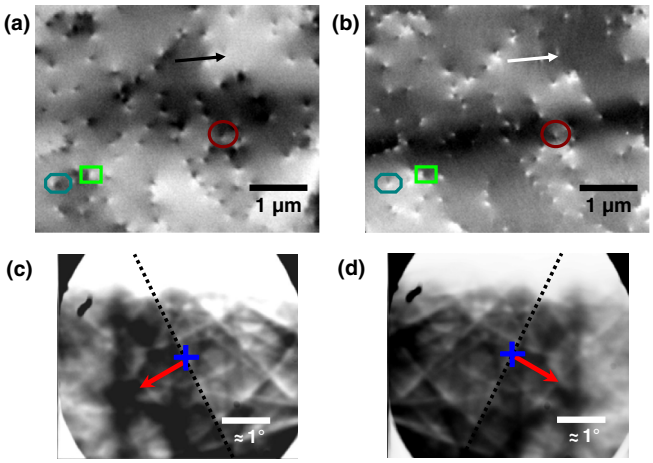

FIG. 3 (color online). Two-beam ECC image and ECP revealing dislocation types: (a) & (b) show ECC images from the same part of the sample acquired at $\boldsymbol{g}$ of (31–4–3) and (–1–34–3), respectively. The circle indicates a screw dislocation, the rectangle an edge dislocation, and the octagon a mixed dislocation. The black and white arrows highlight the change of contrast for subgrains when $\boldsymbol{g}$ is changed. (c) & (d) show the ECPs which correspond to the ECC images shown in (a) & (b). The cross shows the position of the PC, the black dotted lines highlight the diffracting planes and the arrow shows the direction of $\boldsymbol{g}$.

Figures 4(a)–4(h) show high magnification electron channeling contrast images of all the types of TDs. Figures 4(a)–4(d) show images of screw dislocations and show that the direction of their B-W contrast follows $\boldsymbol{g}$ (as discussed previously) and is always orthogonal to the direction of $\boldsymbol{g}$.

There are two possible directions of the B-W contrast observed for screw dislocations for a given $\boldsymbol{g}$, corresponding to screw dislocations with a $\boldsymbol{b}$ of [000 ± 1]. Following the arguments of Edington *et al.* [27] for the identification of screw dislocations—that if the dark lobe (black contrast direction) lies to the left of $\boldsymbol{g}$ then it is a right-handed screw ($\boldsymbol{b}$ [0001]) and if it lies to the left of $\boldsymbol{g}$ then it is a left-handed screw ($\boldsymbol{b}$ [000–1]—we can assign a $\boldsymbol{b}$ of [000–1] to the dislocation shown in Fig. 4(a) and a $\boldsymbol{b}$ of [0001] to the dislocation shown in Fig. 4(c). This argument is valid assuming our $\boldsymbol{g}$ is positive.

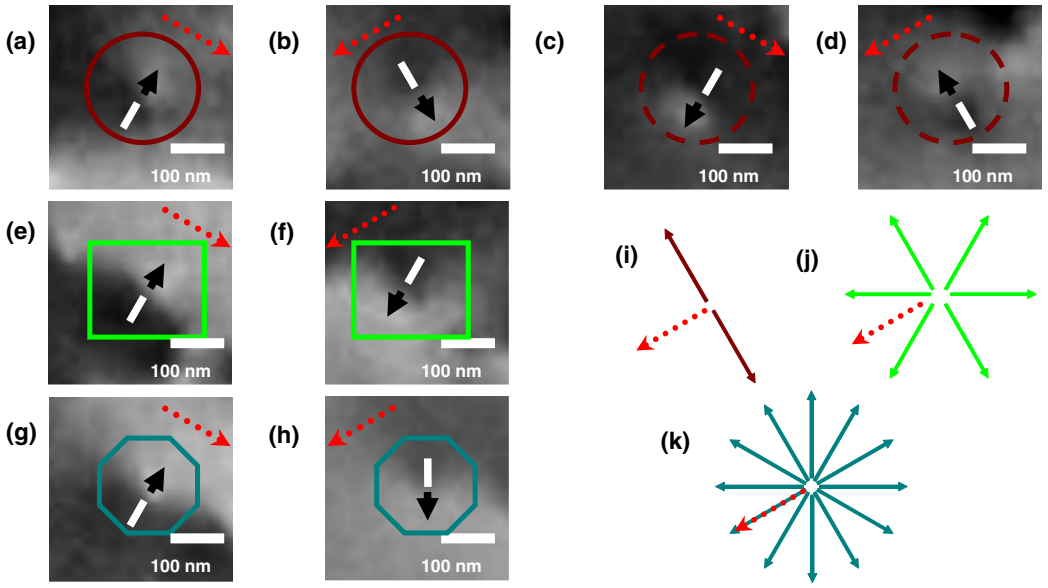

FIG. 4 (color online). Possible B-W contrast directions for TDs: High magnification ECC images showing B-W contrast directions for screw (a)–(d), edge (e)–(f), and mixed (g)–(h) dislocations. (i)–(k) show the possible directions of the B-W contrast of screw (i), edge (j), and mixed dislocations (k) for a $\boldsymbol{g}$ of (31–4–3). The dotted arrow denotes the direction of $\boldsymbol{g}$.

The direction of the B-W contrast for an edge dislocation depends on its $\boldsymbol{b}$ and not on $\boldsymbol{g}$ [22]. The B-W contrast simply reflects the tensile-compressive strain distribution across the edge dislocation [28]. As GaN is a wurtzite semiconductor there are six possible $\boldsymbol{b}$ ($1/3\langle 11\text{–}20\rangle$). We observe six directions of the B-W contrast for the edge dislocations for a given $\boldsymbol{g}$, where the directions are at 60° to each other. Figures 4(e) and 4(f) show the B-W contrast direction for an edge dislocation for the two selected $\boldsymbol{g}$; note that on changing $\boldsymbol{g}$ by 120° the B-W contrast simply reverses.

Finally, for mixed dislocations, b is the vector sum of their edge and screw components; i.e., the $\boldsymbol{b}$ are $1/3\langle 11\text{–}23\rangle$. There are 12 possible $\boldsymbol{b}$ for mixed dislocations. We observe 12 directions of the B-W contrast for the mixed dislocations for a given $\boldsymbol{g}$, with the B-W contrast directions at 30° to each other. For the given $\boldsymbol{g}$, six of the B-W contrast directions observed for the mixed dislocations are the same as that observed for either the screw or edge dislocations; i.e., both the screw and edge dislocations B-W contrast directions overlap with that of a mixed dislocation. Figures 4(i)–4(k) show the schematic of possible B-W contrast directions for screw, edge, and mixed dislocations, respectively, for one $\boldsymbol{g}$ (31–4–3). However, on changing the $\boldsymbol{g}$ [to (–1–34–3)], the change in B-W contrast direction for a mixed dislocation is different to that of either a screw or edge dislocation. This is illustrated in Figs. 4(g) and 4(h) where we show a mixed dislocation whose B-W direction is parallel to that for the screw and edge dislocations shown in Figs. 4(a)–4(c), in the electron channelling contrast image acquired with a $\boldsymbol{g}$ of (31–4–3). On changing the $\boldsymbol{g}$ to (–1–34–3) the B-W contrast direction for the mixed dislocation is no longer perpendicular to that observed for a screw, and the B-W direction is also not observed to reverse its direction as observed for an edge dislocation. The B-W contrast direction for the mixed dislocation is observed to behave differently to that of a screw or edge dislocation when viewed in two images.

Once the dislocations have been identified (we identified 300 dislocations in our images with an uncertainty of less than 2%) it is possible to determine the relative densities of each type of dislocation. The total dislocation density was found to be $3.6 \pm 0.2 \times 10^8$ cm^{-2}. The percentage of pure edge dislocations was ~51% followed by mixed with ~42%. Pure screw dislocations accounted for only ~7% of the total dislocation density. The ratio of the types of individual dislocations depends on the growth conditions and in general screw dislocations are fewer in number when compared to the mixed and edge due to the higher formation energy needed to make them stable. The relative densities of screw to edge as determined here are of the same order (7.3:1 as compared to 5.3:1) to those estimated from x-ray diffraction measurements [29]. Similar analysis has been carried out on nitride thin films produced under different growth conditions.

In summary, ECCI proves to be an ideal nondestructive technique for the quick analysis of the dislocation density and it also gives qualitative information on tilt and twist boundaries. Our approach is a simple, rapid, nondestructive method which can be used to identify dislocation types in GaN and related alloys, and may also be applied to other materials, such as ZnO and SiC, with the wurtzite crystal structure.

This work is carried out with the partial support of the EU under the ITN RAINBOW (http://rainbow.ensicaen.fr/),

Grant Agreement No: PITN-GA-2008-213238 and EPSRC Grant No: EP/D058686/1. P. J. P. acknowledges support from Science Foundation Ireland under Grant No. 07/SK/I1258b.

*Now at Tyndall National Institute, University College Cork, "Lee Maltings", Cork, Ireland.
†C.Trager-Cowan@strath.ac.uk

[1] D. C. Look and J. R Sizelove, Phys. Rev. Lett. **82**, 1237 (1999).
[2] X. H. Wu, L. M. Brown, D. Kapolnek, S. Keller, B. Keller, S. P. DenBaars, and J. S. Speck, J. Appl. Phys. **80**, 3228 (1996).
[3] W. R. Liu, W. F. Hsieh, C. H. Hsu, K. S. Liang, and F. S. Chien, J. Appl. Crystallogr. **40**, 924 (2007).
[4] F. A. Ponce, D. Cherns, W. T. Young, and J. W. Steeds, Appl. Phys. Lett. **69**, 770 (1996).
[5] D. M. Follstaedt, N. A. Missert, D. D. Koleske, C. C. Mitchell, and K. C. Cross, Appl. Phys. Lett. **83**, 4797 (2003).
[6] R. Datta, M. J. Kappers, J. S. Barnard, and C. J. Humphreys, Appl. Phys. Lett. **85**, 3411 (2004).
[7] D. A. Wood, P. J. Parbrook, P. A. Lynch, M. Lada, and A. G. Cullis, Phys. Status Solidi A **188**, 641 (2001).
[8] C. Trager-Cowan, F. Sweeney, P. W. Trimby, A. P. Day, A. Gholinia, N.-H. Schmidt, P. J. Parbrook, A. J. Wilkinson and I. M. Watson, Phys. Rev. B **75**, 085301 (2007).
[9] B. A. Simpkin and M. A. Crimp, Ultramicroscopy **77**, 65 (1999).
[10] D. B. Williams and C. B. Carter, *Transmission Electron Microscopy: A Textbook for Materials Science* (Springer, New York, 2009), Chap. 19.
[11] L. M. Peng, S. L. Dudarev, and M. J. Whelan, *High Energy Electron Diffraction and Microscopy* (Oxford University Press, Oxford, 2003), Chap. 2.
[12] A. Winkelmann, C. Trager-Cowan, F. Sweeney, A. P. Day, and P. J. Parbrook, Ultramicroscopy **107**, 414 (2007).
[13] P. Morin, M. Pitaval, D. Besnard, and G. Fontaine, Philos. Mag. A **40**, 511 (1979).
[14] D. C. Joy, D. E. Newbury, and D. L. Davidson, J. Appl. Phys. **53**, R81 (1982).
[15] A. J. Wilkinson and P. B. Hirsch, Micron **28**, 279 (1997).
[16] H. Watanabe, N. Kuroda, H. Sunakawa, and A. Usui, Appl. Phys. Lett. **77**, 1786 (2000).
[17] N. Osakabe, Y. Tanishiro, K. Yagi, and G. Honjo, Surf. Sci. **102**, 424 (1981).
[18] Y. N. Picard and M. E. Twigg, J. Appl. Phys. **104**, 124906 (2008).
[19] M. A. Crimp, B. A. Simpkin and B. C. Ng, Philos. Mag. Lett. **81**, 833 (2001).
[20] W. J. Tunstall, P. B. Hirsch, and J. Steeds, Philos. Mag. **9**, 99 (1964).
[21] Y. N. Picard, J. D. Caldwell, M. E. Twigg, C. R. Eddy, Jr., M. A. Mastro, R. L. Henry, R. T. Holm, P. G. Neudeck, A. J. Trunek, and J. A. Powell, Appl. Phys. Lett. **91**, 094106 (2007).
[22] Y. N. Picard, M. E. Twigg, J. D. Caldwell, C. R. Eddy Jr., M. A. Mastro, and R. T. Holm, Scr. Mater. **61**, 773 (2009).
[23] J. W. P. Hsu, M. J. Manfra, R. J. Molnar, B. Heying, and J. S. Speck, Appl. Phys. Lett. **81**, 79 (2002).
[24] B. S. Simpkins, E. T. Yu, P. Waltereit, and J. S. Speck, J. Appl. Phys. **94**, 1448 (2003).
[25] S. I. Maximenko, J. A. Freitas, Jr., R. L. Myers-Ward, K.-K. Lew, B. L. VanMil, C. R. Eddy, Jr., D. K. Gaskill, P. G. Muzykov, and T. S. Sudarshan, J. Appl. Phys. **108**, 013708 (2010).
[26] S.-H. Lim, D. Shindo, H.-B. Kang, and K. Nakamura, J. Cryst. Growth **225**, 202 (2001).
[27] J. W. Edington, *Practical Electron Microscopy in Materials Science* (Macmillan, London, 1976), Chap. 3.
[28] E. Ruedl, P. Delavignette, and S. Amelinckx, J. Nucl. Mater. **6**, 46 (1962).
[29] T. A. Lafford, P. J. Parbrook, and B. K. Tanner, Phys. Status Solidi C **0**, 542 (2003).